

# ULTRA-LIGHT AXION DARK MATTER AND ITS IMPACTS ON DARK HALO STRUCTURE IN $N$ -BODY SIMULATION

JIAJUN ZHANG

School of Physics and Astronomy, Shanghai Jiao Tong University, Shanghai, China  
and

Department of Physics, The Chinese University of Hong Kong, Hong Kong, China

YUE-LIN SMING TSAI

Physics Division, National Center for Theoretical Sciences, Hsinchu, Taiwan

JUI-LIN KUO

Department of Physics, National Tsing Hua University, Hsinchu, Taiwan

KINGMAN CHEUNG

Physics Division, National Center for Theoretical Sciences, Hsinchu, Taiwan

Department of Physics, National Tsing Hua University, Hsinchu, Taiwan

and

Division of Quantum Phases and Devices, School of Physics, Konkuk University, Seoul 143-701, Republic of Korea

MING-CHUNG CHU

Department of Physics, The Chinese University of Hong Kong, Hong Kong, China

## ABSTRACT

The Ultra-Light Axion (ULA) is a dark matter candidate with mass  $\mathcal{O}(10^{-22})$  eV and de Broglie wavelength of order kpc. Such an axion, also called the Fuzzy Dark Matter (FDM), thermalizes via the gravitational force and forms a Bose-Einstein condensate. Recent studies suggested that the quantum pressure from the FDM can significantly affect the structure formation in small scales, thus alleviating the so-called “small-scale crisis”. In this paper, we develop a new technique to discretize the quantum pressure and illustrate the interactions among FDM particles in the  $N$ -body simulation, which accurately simulates the formation of the dark-matter halo and its inner structure in the region outside the softening length. In a self-gravitationally-bound virialized halo, we find a constant density, solitonic core, which is consistent with the theoretical prediction. The existence of the solitonic core reveals the non-linear effect of quantum pressure and impacts the structure formation in the FDM model.

## 1. INTRODUCTION

There have been many compelling evidences for the existence of cold dark matter (CDM), which successfully explains the rotation curves of spiral galaxies, the Cosmic Microwave Background power spectrum, the Bullet Cluster, and large scale structure formation of the Universe. The most well-motivated model for CDM is the weakly interacting massive particles (WIMPs), whose mass range is from the sub-GeV to 100 TeV owing to the relic density requirement. Unfortunately, up to now no compelling evidence of WIMPs was found in all different types of searches, such as collider searches (Aaboud et al. 2016; CMS 2016), underground detections (Akerib et al. 2016; Tan et al. 2016), and astronomical observations (Ackermann et al. 2015; Aartsen et al. 2016). Null signals reported in all these experiments have shrunk the parameter space of many WIMP models to some finely-tuned regions. Also, the next generation of CDM searches are shifting their focuses to different mass regions.

The CDM model through detailed  $N$ -body simulations, though successfully explains the observations in large scales, fails to account for the observations in relatively smaller scales; this is known as the “small-scale crisis”: (i) the missing satellites problem (Moore et al. 1999; Klypin et al. 1999), (ii) the cusp-core problem (de Blok 2010), and (iii) the too-big-to-fail problem (Boylan-Kolchin et al. 2011). In order to alleviate the problems, two types of mechanism are introduced. Some authors believe that the problems can be alleviated by considering baryonic feedback carefully (Schaller et al. 2015a,b). Others believe that a new mechanism of velocity boost is needed for the DM momentum exchange beyond the collisionless picture of the CDM. Examples include strongly self-interacting DM (Tulin et al. 2013), Fuzzy Dark Matter (FDM) (Hu et al. 2000a), etc. Both of them share the the feature of smoothing out the cuspy matter distribution.

The Ultra-Light Axion (ULA) or so-called Fuzzy Dark Matter (FDM) is then a good candidate for CDM (Turner 1983; Press et al. 1990; Sin 1994; Goodman 2000; Peebles 2000; Matos et al. 2002; Guzmán & Ureña-López 2003; Amendola & Barbieri 2006; Calabrese & Spergel 2016; Kim & Marsh 2016). It not only keeps the success of CDM in dealing with large-scale issues, but also provides a possible solution to the small-scale crisis. The FDM is a scalar boson with an extremely light mass  $\gtrsim 10^{-22}$  eV, which is required by a recent observation on the reionization history of the Universe (Bozek et al. 2015). A recent discussion about the constraints on the FDM mass from CMB can be found in Ref. (Hložek et al. 2017). With a common velocity in the order of  $100 \text{ km s}^{-1}$ , the de Broglie wavelength of the FDM is very long  $\sim \mathcal{O}(\text{kpc})$  (Sin 1994; Hu et al. 2000a; Ferrer & Grifols 2004; Boehmer & Harko 2007; Lee & Lim 2010; Sikivie & Yang 2009; Mielke & Perez 2009; Chavanis 2011; Chavanis & Delfini 2011; Dev et al. 2016; Marsh 2016). Some authors suggested that the FDM is in Bose-Einstein Condensate (BEC) (Schive et al. 2014a). However it is still an open question, because the BEC transition temperature is higher than the cosmological temperature. Hence, in this paper we will not join such a debate but instead focus on numerically solving the structure formation of the FDM model efficiently. The FDM is non-thermally produced and thus still in the non-relativistic regime and behaves like CDM. However, due to the quantum nature of the FDM in small scales, about tens or hundreds of kpc, remarkably the FDM is distinguishable from the normal CDM. One can find those differences in the matter power spectrum (Veltmaat & Niemeyer 2016), halo mass function (HMF) (Du et al. 2016), and halo structure (Schwabe et al. 2016). The most striking feature of the FDM is that the halo has a solitonic core of size  $\sim \mathcal{O}(\text{kpc})$  resulting from the quantum pressure of the FDM particles, which can be larger than their self-gravity. Hence, the quantum pressure plays an essential role in solving the small-scale crisis. Moreover, if the halo small scale structure can be measured more accurately in the future, the FDM particle mass can be constrained. The latest reviews are given in Ref. (Marsh 2016; Hui et al. 2016).

In this work, we propose a new scheme – the effective Particle-Particle (PP) interaction – for simulating the FDM model, by which one can compute the quantum effect of the FDM in the  $N$ -body simulation with high resolution. In a self-gravitationally-bound virialized halo, we find a constant density core – solitonic core – of size of around 1 kpc, but with a lower density than that in the conventional CDM model. The result shows the non-trivial quantum pressure effect on the structure formation. We present the effects of the linear and non-linear power spectrum growth, especially for the non-linear effect in high density regions. For small scale structures, particularly for scales smaller (larger) than one de Broglie wavelength, the quantum pressure is attractive (repulsive). This leads to non-trivial structure formation in high density regions. However, in early age, low over-density regions, the linear effect is mainly from the repulsive quantum pressure which suppresses the matter power spectrum at scales smaller than the Jeans scale.

We have developed an independent and completely different simulation scheme compared to a few previous studies, which were based on direct cosmological simulations with the Schrödinger-Poisson equations (Schive et al. 2014a), Smoothed Particle Hydrodynamic (SPH) scheme simulation technique (Mocz & Succi 2015) and Particle-Mesh (PM) scheme simulation technique (Veltmaat & Niemeyer 2016). We cross-check our results with previous simulations and find them consistent with each other. Nevertheless, our implementation of the quantum effect with a simple PP method helps us to explain some of the previously unclear behavior and understand self-consistently how quantum pressure affects the structure formation.

The main advantage of our scheme is its high running efficiency. From all the tests that we have performed, the CPU time required for the FDM simulations is only two to three times longer than the corresponding CDM simulations, which is well expected for our method described here. Thus, we can perform cosmological simulation in larger scale than previous literature with the same amount of computational resources (Schive et al. 2014a; Mocz & Succi 2015; Veltmaat & Niemeyer 2016).

The following sections are arranged as follows. In Sec. 2, we introduce the theoretical approach of the effective Particle-Particle interaction. In Sec. 3, we describe the simulation setup and discuss the results. Finally, we summarize our outcomes in Sec. 4.

## 2. METHODOLOGY

### 2.1. Schrödinger-Poisson equations

The nature of FDM can be well described by the Schrödinger-Poisson equations,

$$i\hbar \frac{d\Psi}{dt} = -\frac{\hbar^2}{2m_\chi} \nabla^2 \Psi + m_\chi V \Psi, \quad (1)$$

and

$$\nabla^2 V = 4\pi G m_\chi |\Psi|^2. \quad (2)$$

Here  $\hbar$ ,  $m_\chi$  and  $V$  are the Planck constant, particle mass and the gravitational potential acting on a particle, respectively. The wave function  $\Psi$  can be written as <sup>1</sup>

$$\Psi = \sqrt{\frac{\rho}{m_\chi}} \exp\left(\frac{iS}{\hbar}\right) \quad (3)$$

in terms of the number density  $\frac{\rho}{m_\chi}$ , while we can define the gradient of  $S$  to be the DM momentum,

$$\nabla S = m_\chi \mathbf{v}. \quad (4)$$

After solving the Schrödinger-Poisson equations, from the real and imaginary parts of the solution, one can obtain the continuity equation,

$$\frac{d\rho}{dt} + \nabla \cdot (\rho \mathbf{v}) = 0, \quad (5)$$

and the momentum-conservation equation,

$$\frac{d\mathbf{v}}{dt} + (\mathbf{v} \cdot \nabla) \mathbf{v} = -\nabla(Q + V), \quad (6)$$

where we have defined the quantum pressure as

$$Q = -\frac{\hbar^2}{2m_\chi^2} \frac{\nabla^2 \sqrt{\rho}}{\sqrt{\rho}}. \quad (7)$$

Eqs. (5) and (6) are known as Madelung equations (Spiegel 1980; Uhlemann et al. 2014; Marsh 2015). One can see that such a pressure is only related to the mass density  $\rho$  and can be treated as a new force on the particles additional

<sup>1</sup> The original FDM paper Hu et al. (2000b) has a factor 1/2 in the wave function for identical dark matter particles. However, this normalization factor will not change the Lagrangian density and the size of quantum pressure in our study.

to gravity. Later, we shall focus on this pressure term and discuss how to obtain the acceleration information by using the Hamiltonian field theory.

To discuss the effect of the quantum pressure, we can start with the Hamiltonian without the gravity term,

$$H = \int \frac{\hbar^2}{2m_\chi} |\nabla\Psi|^2 d^3x = \int \frac{\rho}{2} |\mathbf{v}|^2 d^3x + \int \frac{\hbar^2}{2m_\chi^2} (\nabla\sqrt{\rho})^2 d^3x. \quad (8)$$

We can write the kinetic energy term in discretized form with particle index  $j$

$$T = \int \frac{\rho}{2} |\mathbf{v}|^2 d^3x = \sum_j \frac{1}{2} m_j \left( \frac{dq_j}{dt} \right)^2, \quad (9)$$

where  $q_j$  is the coordinate of the  $j$ th particle, and the effective potential energy is from the quantum pressure

$$K_\rho = \int \frac{\hbar^2}{2m_\chi^2} (\nabla\sqrt{\rho})^2 d^3x. \quad (10)$$

Note that we did not discretize  $K_\rho$  here but delay it to the next subsection because it will require some efforts to do so. Based on  $T$  and  $K_\rho$  the Lagrangian of the system without gravity is

$$L = T - K_\rho = \sum_j \frac{1}{2} m_j \left( \frac{dq_j}{dt} \right)^2 - \int \frac{\hbar^2}{2m_\chi^2} (\nabla\sqrt{\rho})^2 d^3x, \quad (11)$$

and the Euler-Lagrangian equation becomes

$$\frac{d}{dt} \frac{\partial L}{\partial \dot{q}_j} - \frac{\partial L}{\partial q_j} = 0 \implies m_j \ddot{q}_j = - \frac{\partial K_\rho}{\partial q_j}. \quad (12)$$

One can see that the  $\rho$  in  $K_\rho$  is a continuous function, which cannot be used in the PP method. Therefore, the major task is to further discretize the continuous function  $\partial K_\rho / \partial q_j$ , which we shall describe in more details in the next subsection. We clarify here that, the index  $i$  and  $j$  here are representing the simulation particles rather than single "Ultra-Light Axion" particles.

## 2.2. Particle-particle implementation of quantum pressure

For a particle-particle interaction system, the number density for each individual particle is a delta function. Intuitively, the mass density  $\rho$  can be discretized as

$$\rho(\mathbf{r}) = \sum_i m_i \delta(\mathbf{r} - \mathbf{r}_i), \quad (13)$$

where the summation over the index  $i$  means to add up all the particles. Numerically, treatment of a delta function is a difficult computational problem because of the sampling coverage issue. However, conventionally one can approximate a delta function as a narrow Gaussian/kernel function, as long as the width is small enough. The reasons and advantages to use the Gaussian smoothing kernel are listed as follows. (i) It naturally keeps the kernel smooth, differentiable, and spherically symmetric. (ii) The particle-particle interaction can naturally avoid the singularity at zero-density positions. Because of the finite grid size, such a singularity can numerically make the results unphysical. Specifically, we write down the form of the delta function as

$$\delta(\mathbf{r} - \mathbf{r}_i) = \frac{2\sqrt{2}}{\lambda^3 \pi^{3/2}} \exp\left(-\frac{2|\mathbf{r} - \mathbf{r}_i|^2}{\lambda^2}\right), \quad (14)$$

with a narrow width  $\lambda$ . Note that the value of  $\lambda$  is not arbitrary and should be the same as the de Broglie wavelength because one FDM particle has to be found with a high probability within a Gaussian wave packet, motivated by the wave function Eq. (3). In our work, the probability of finding a FDM in one wavelength is set at 95%.

Taking the FDM mass around  $\mathcal{O}(10^{-31})$  GeV as an example, its wavelength  $\lambda$  is order of kpc. Inserting Eq. (14)

back to the  $(\nabla\sqrt{\rho})^2$  term in Eq. (10), the expression can be expanded by using the kernel function,

$$\begin{aligned} [\nabla\sqrt{\rho(\mathbf{r})}]^2 &= \frac{1}{4\rho(\mathbf{r})} \left[ \sum_i m_i \nabla\delta(\mathbf{r} - \mathbf{r}_i) \right]^2, \\ &= \frac{1}{4\rho(\mathbf{r})} \left[ \sum_i m_i \delta(\mathbf{r} - \mathbf{r}_i) \left(-\frac{4}{\lambda^2}\right)(\mathbf{r} - \mathbf{r}_i) \right]^2, \\ &= \frac{4}{\lambda^4\rho(\mathbf{r})} \left[ \sum_i m_i \delta(\mathbf{r} - \mathbf{r}_i)(\mathbf{r} - \mathbf{r}_i) \right]^2. \end{aligned} \quad (15)$$

In the simulation, those FDM particles such as axions will be grouped into a big mass clump in space which can be treated as an imaginary particle point (neglecting the size of the clump in the cosmological scale), and the mass density, Eq. (13), becomes

$$\rho(\mathbf{r}) = \sum_j \sum_i m_i \delta(\mathbf{r} - \mathbf{r}_j), \quad (16)$$

with the index  $j$  for each imaginary particle clump. Mathematically, one can think that the mass density is expanded around  $\mathbf{r}_j$  to include all the FDM particles,  $\mathbf{r} \rightarrow \mathbf{r} - \mathbf{r}_j$  and  $\mathbf{r}_i \rightarrow \mathbf{r}_i - \mathbf{r}_j$ . Given such a consideration, the summation of individual FDM particles is effectively the same as summing over all the imaginary particle points, and Eq. (15) can be further polished to be

$$[\nabla\sqrt{\rho(\mathbf{r})}]^2 \simeq \frac{4}{\lambda^4} \left[ \sum_j m_j \delta(\mathbf{r} - \mathbf{r}_j)(\mathbf{r} - \mathbf{r}_j) \right]^2 \left[ \sum_j m_j \delta(\mathbf{r} - \mathbf{r}_j) \right]^{-1}. \quad (17)$$

It is worth mentioning that the form in Eq. (17) is identical to Eq. (15) but their meanings should not be confused. Hence, we leave the different indices here. At this stage, we have successfully converted the Gaussian wave packet into an imaginary particle-smoothing kernel.

To completely discretize  $\partial K_\rho/\partial q_j$ , we still need to integrate Eq. (17) over all space. Due to the nature of the delta function, we just need to focus on the volume surrounding the imaginary particle points. Therefore, the integration together with kernel approach gives

$$\int [\nabla\sqrt{\rho(\mathbf{r})}]^2 dx^3 \simeq \int \frac{4dx^3}{\lambda^4} \left[ \sum_j m_j \delta(\mathbf{r} - \mathbf{r}_j)(\mathbf{r} - \mathbf{r}_j) \right]^2 \left[ \sum_j m_j \delta(\mathbf{r} - \mathbf{r}_j) \right]^{-1} \quad (18)$$

$$\simeq 4\lambda^{-4} \sum_j m_j \delta(\mathbf{r} - \mathbf{r}_j)(\mathbf{r} - \mathbf{r}_j)^2 \Delta V_j \mathcal{B}_j \quad (19)$$

$$\simeq 4\lambda^{-4} \sum_j m_j \frac{\Delta V_j \mathcal{B}_j}{\lambda^3 \pi^{3/2}} \exp\left[-\frac{(\mathbf{r} - \mathbf{r}_j)^2}{\lambda^2}\right] (\mathbf{r} - \mathbf{r}_j)^2, \quad (20)$$

where the parameters  $\Delta V_j$  and  $\mathcal{B}_j$  are the effective volume and correction factor of the  $j$ th simulation particle which will be described in more detail below.

We propose a correction factor  $\mathcal{B}_j$  for the  $j$ th simulation particle in order to numerically take care of the different integration results between the delta function and Gaussian kernel. In other words, when we treat a delta function as one Gaussian kernel with width equal to one matter wavelength, it does not behave like a delta function in the region where the distance between two kernel centers is less than one wavelength. In such a short range, the overlap between two Gaussian tails can also contribute significantly, especially when performing integration with high particle density. For more detailed explanations and the fitting formula for  $\mathcal{B}_j$  Eq. (A5), see Appendix A.

Theoretically, the effective volume  $\Delta V_j$  for each simulation particle  $j$  is of the order of  $\lambda^3 \pi^{3/2}$  resulting from a Gaussian kernel integral. However, the exact value of  $\Delta V_j$  can differ from system to system because of the complexity of the inner kernel region. Hence, we treat it as a phenomenological free parameter (a constant for simplicity), but we

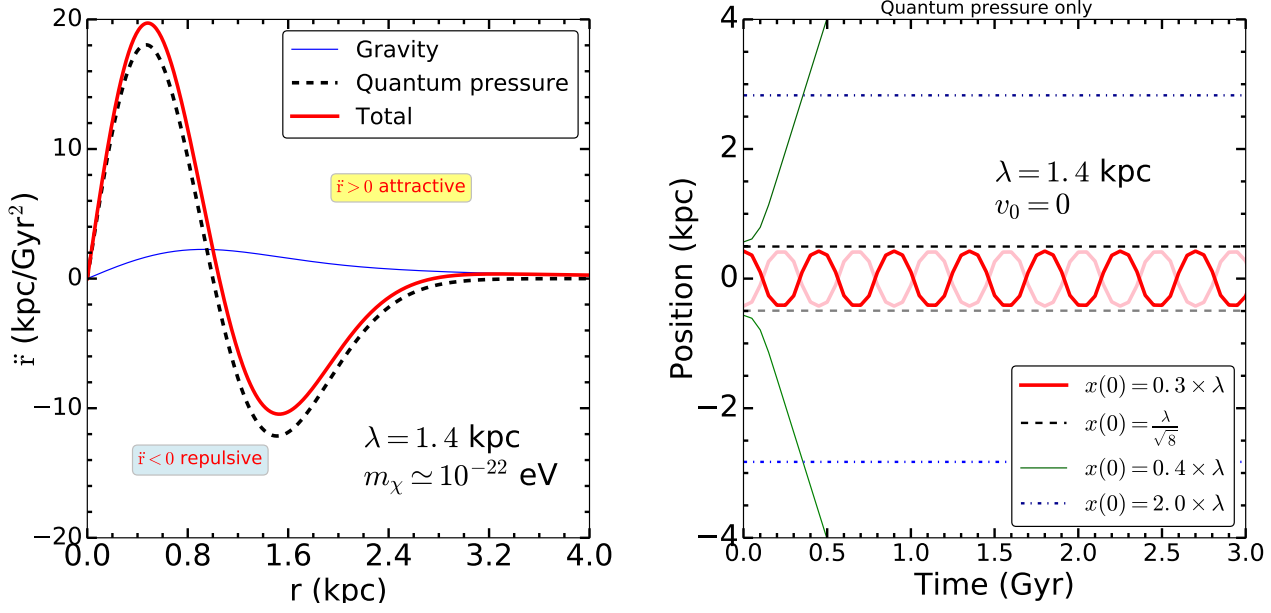


**Figure 1.** Left panel: the acceleration from quantum pressure (black dashed), gravity (blue solid), and their sum (red solid) between two particles. The x-axis is the distance between two particles while the y-axis is the acceleration. Right panel: the particle position, which is changing due to the quantum pressure, vs. time. The red-solid, black-dashed, green-solid, and blue-dash-dotted lines represent the solutions with initial positions at  $0.3\lambda$ ,  $\lambda/\sqrt{8}$ ,  $0.4\lambda$ , and  $2\lambda$ , respectively. However, the light color lines represent their partner particles located at the opposite side  $-0.3\lambda$ ,  $-\lambda/\sqrt{8}$ ,  $-0.4\lambda$ , and  $-2\lambda$  initially.

adjust its value to match the result inside the soliton core obtained by other approaches which have better resolution in the region less than one wavelength, such as Ref. [Schive et al. \(2014a\)](#).

Finally, Eq. 10 can be simply rearranged as

$$\sum_j \frac{\partial K_\rho}{\partial q_j} = \frac{4\hbar^2}{m_\chi^2 \lambda^4} \sum_j m_j \Delta V_j \mathcal{B}_j \exp\left[-\frac{2|\mathbf{r} - \mathbf{r}_j|^2}{\lambda^2}\right] \left(1 - \frac{2|\mathbf{r} - \mathbf{r}_j|^2}{\lambda^2}\right) (\mathbf{r} - \mathbf{r}_j), \quad (21)$$

and the equation of motion, Eq. (12), becomes

$$\sum_j m_j \ddot{\mathbf{q}} = -\frac{4\hbar^2}{m_\chi^2 \lambda^4} \sum_j m_j \Delta V_j \mathcal{B}_j \exp\left[-\frac{2|\mathbf{r} - \mathbf{r}_j|^2}{\lambda^2}\right] \left(1 - \frac{2|\mathbf{r} - \mathbf{r}_j|^2}{\lambda^2}\right) (\mathbf{r} - \mathbf{r}_j). \quad (22)$$

Substituting  $q$  with  $\mathbf{r}$ , the additional acceleration from quantum pressure used in the simulation can be written as

$$\ddot{\mathbf{r}} = \frac{4M\hbar^2}{M_0 m_\chi^2 \lambda^4} \sum_j \mathcal{B}_j \exp\left[-\frac{2|\mathbf{r} - \mathbf{r}_j|^2}{\lambda^2}\right] \left(1 - \frac{2|\mathbf{r} - \mathbf{r}_j|^2}{\lambda^2}\right) (\mathbf{r}_j - \mathbf{r}). \quad (23)$$

Here  $M$  is the mass of the simulation particle and  $M_0$  is a normalization factor accounting for the size of  $\Delta V_j$ , which we choose to be  $10^6 M_\odot$ . Interestingly, if we put any “one” test particle around some quantum pressure sources, the additional energy to the system injected from quantum pressure term is zero. Namely, the total work, the integration of Eq. (23) from  $r = 0$  to  $r = \infty$ , vanishes.

To illustrate the effect of quantum pressure, let us consider a two-particle system ( $\mathcal{B}_j = 1$ ) separated by a distance of order  $\mathcal{O}(\text{kpc})$  and the acceleration caused by quantum pressure will be  $\mathcal{O}\left(\frac{\hbar^2}{m^2 \lambda^3}\right) \sim \mathcal{O}(10^{-10} m/s^2)$ . In the left panel of Fig. 1, we demonstrate the effect of quantum pressure in the plane of  $(r, \dot{r})$ . The acceleration from quantum pressure, gravity, and the sum are shown by the black dashed line, blue line, and red line, respectively. Clearly, the quantum pressure can be attractive (positive sign in our definition)<sup>2</sup> if the distance between two particles

<sup>2</sup> Here the terminology “attractive” and “repulsive” are just simple phrases to describe the quantum pressure being positive or negative, respectively.

is less than  $\lambda/\sqrt{2}$ . However, it becomes repulsive (negative sign in our definition) if the distance is greater than  $\lambda/\sqrt{2}$ . To understand this, we refer back to the quantum pressure definition in Eq. (7). The pressure term  $Q$  is proportional to the second derivative of the mass density, namely, the curvature of the density, which can have negative, positive, or zero values, physically corresponding to attractive, repulsive, and zero forces.

In the right panel of Fig. 1, we show the position  $x(t)$  of one of the particles in this two-particle system as a function of time by solving Eq. (23). Here the origin is located at the center of mass and such that  $r(t) = 2x(t)$ . The red-solid, black-dashed, green-solid, and blue-dash-dotted lines present the cases with initial positions  $x(0)$  at  $0.3\lambda$ ,  $\lambda/\sqrt{8}$ ,  $0.4\lambda$ , and  $2\lambda$ , respectively. Also, the position of the other particle is drawn in the corresponding lighter colors for reference. Interestingly, when the distance between the two particles is smaller than  $\lambda/\sqrt{2}$ , the attractive force will bound them. Note that this also demonstrates the phenomenon of Bose-Einstein condensation. One shall bear in mind that for fermionic particles such short range attractive forces would not exist because of the Pauli's Exclusion Principle. However, the repulsive force will push these two particles away for  $\frac{\lambda}{\sqrt{2}} < r(0) < \sqrt{2}\lambda$ . At  $r(0) = \lambda/\sqrt{2}$ , the node represents zero interaction. For the  $x(0) \gg \sqrt{2}\lambda$  case, the two particles barely feel the force from each other so that they will continue with their initial velocities, though we set them to be zero.

This reveals the quantum pressure as a short-range interaction, shown in Eq. (23), with the exponentially decaying term.

### 3. NUMERICAL RESULT

**Gadget2** (Springel 2005) is a **TreePM** hybrid N-body code. However, in order to describe continuous quantum pressure, the interaction term has to be discretized as we have discussed in the previous section. Therefore, we modified **Gadget2** to compute the contribution from the quantum pressure. In this section, we first describe the details of what we used in our simulation, and then we present our simulation results.

#### 3.1. The simulation setup

The PM method is mostly useful for cosmological simulations with periodic boundary conditions. As we have seen from the previous section that the quantum pressure behaves like a short-range interaction, we therefore keep the original PM code which takes care of the long-range force calculation. However, we have to use the Tree method to take care of the short-range force calculation, and so the part of Tree force calculation in **Gadget2** has to be modified to include the quantum pressure term. Finally, we do not need to set softening for the quantum pressure acceleration since it is finite in the  $(\mathbf{r}_j - \mathbf{r}) \simeq 0$  region.

To study the differences between the CDM and FDM, we set up a self-collapsing system. A cubic box with a side length 400 kpc is generated with totally  $10^6$  simulation particles homogeneously distributed inside the box with the vacuum boundary condition. The box can be understood as an over-density region which will collapse under its self-gravity. Each simulation particle consists of a  $10^6$  solar mass. All particles start from rest and the system collapses resulting from their self-gravity to form a stable self-gravitationally-bound virialized halo at the center. It is sufficient to stop the simulation around 10 Gyr. The final stable virialized halo in FDM model depends sensitively on the initial slight perturbation given to the system.

Two kinds of **Gadget2** simulations are performed: one with the modified code for FDM quantum pressure effect and the other one with the original **Gadget2** code. In both simulations, we use the same initial conditions, and the gravitational softening length is chosen to be 0.89 kpc. The ULA mass and wavelength are fixed to be  $2.5 \times 10^{-22}$  eV and 1.4 kpc, respectively. We further run several simulations with different softening lengths in order to make sure that the final density and velocity distributions of the halos have converged.

#### 3.2. Simulation results

In Fig. 2, we present the particle distributions of our simulations for a self-gravitationally-collapse system. The three panels on the upper (lower) row are for the CDM (FDM) scenario. The figures from the left to right panels are

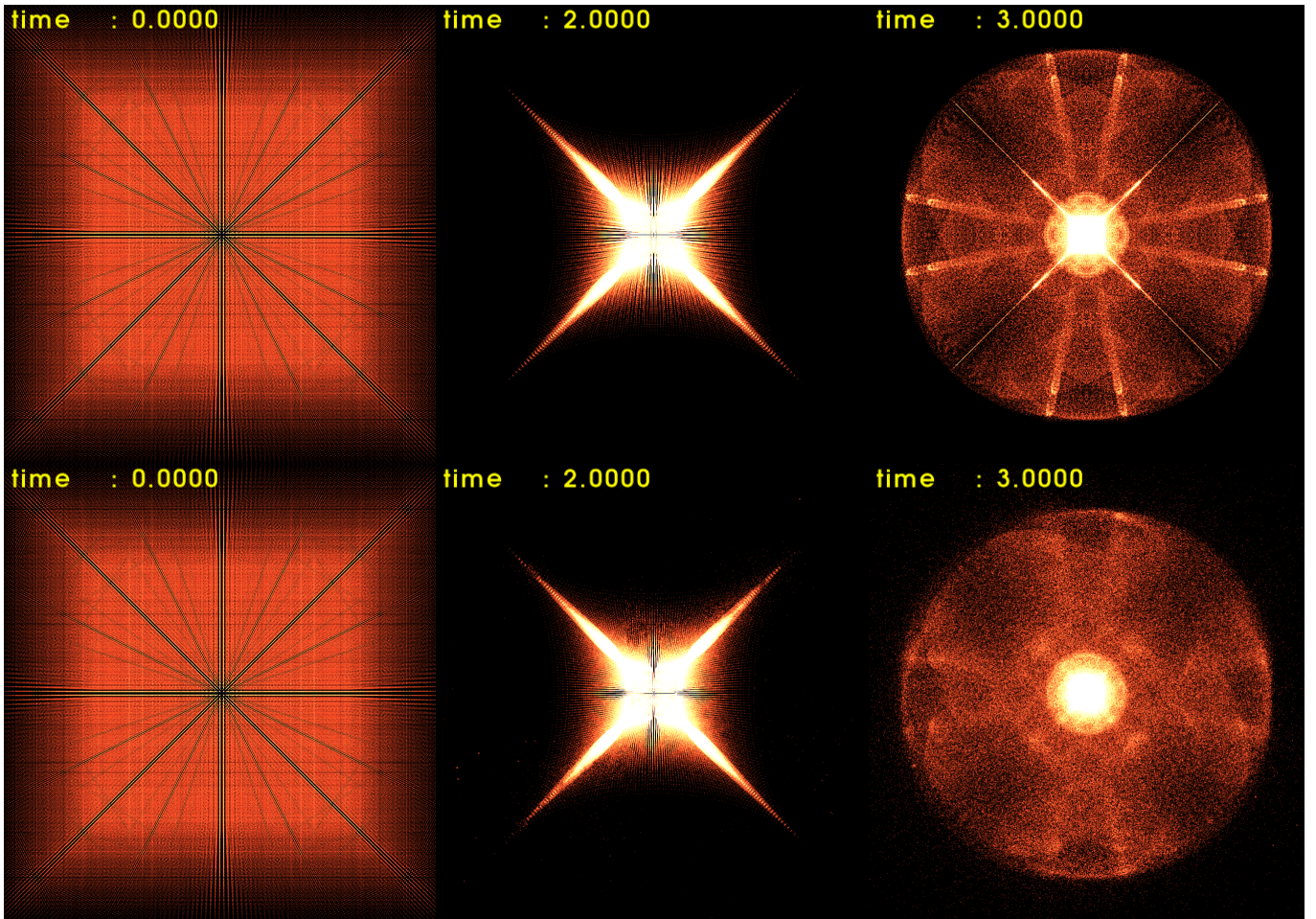


**Figure 2.** The particle distributions of the CDM (on the top) and FDM (on the bottom) simulations for a self-gravitationally-collapse system. The labels at the upper left corner show the time in Gyr.

two-dimensional slices at the evolution time 0, 2, and 3 Gyr. Clearly, the distribution of FDM is more smooth and spread out than the CDM case, especially at later time. This is exactly the novel feature of the quantum pressure.

To further illustrate the effect of the quantum pressure on the halo density profile, we plot the mass enclosed in 8 kpc in the left panel of Fig. 3, which shows the core mass evolution along the time direction in unit of Gyr for the CDM (blue line) and FDM (red solid line) cases. For reference we also plot two curves colored in pink (thin dashed) for  $\mathcal{B}_j = 1$  case.<sup>3</sup> Both systems of CDM and FDM will be in the equilibrium state after 3 – 4 Gyr when the mass within 8 kpc does not change significantly. Note that the FDM halo possesses slightly less (about 80% of the) mass inside 8 kpc than the CDM one, due to the quantum pressure. The FDM halo is also slowly losing mass inside 8 kpc even after 4 Gyr while the CDM is already stable. However both FDM halo and CDM halo are fully virialized after 4 Gyr, their overall density profiles are stable.

In the right panel of Fig. 3, we show the rotational curves for the FDM (red solid line for FDM including correction  $\mathcal{B}_j$  but pink thin dashed lines for FDM without correction as references) and CDM (blue line) halo after 10 Gyr evolution. We take this halo as an example because it is fully virialized. We can see that inside 3 kpc the circular velocity for the FDM halo is always smaller than that of the CDM halo. This implies that the FDM halo has a lower density in the inner core than that of the CDM. Note that the green shaded region represents the softening length 0.89 kpc and we should treat it as our numerical simulation resolution boundary, inside which we should not

<sup>3</sup> Because of the algorithm of the tree method used in Message Passing Interface (MPI), the boundary of the simulation grid can be slightly different. Without implementing the correction factor  $\mathcal{B}_j$ , such small differences from Gaussian tails can be accumulated and developed into two different but stable results by using several different node assignments.

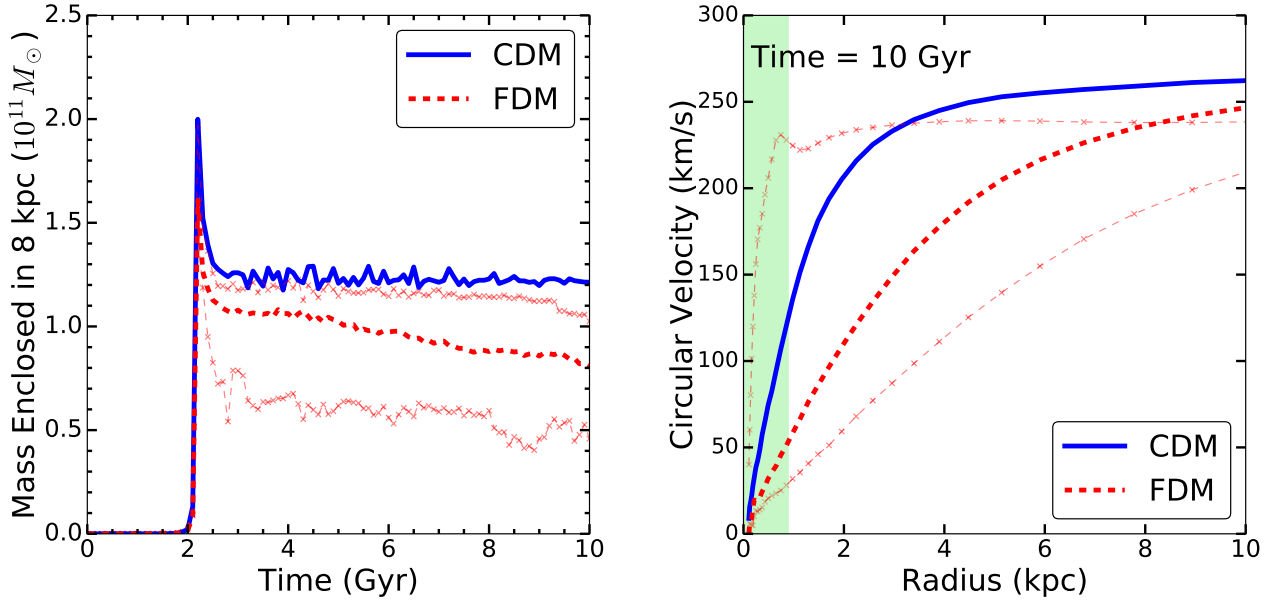


**Figure 3.** The evolution of mass enclosed in 8 kpc from the center is shown on the left panel. After 3 – 4 Gyr evolution, the self-collapse system reaches equilibrium for both CDM and FDM models. The right panel shows the final rotational curve. The circular velocity for the FDM halo is smaller than the CDM inside 10 kpc from the center. Two solutions of FDM without corrections (pink thin solid lines) are shown for reference. The green shaded region represents the radius of halo smaller than the softening length 0.89 kpc.

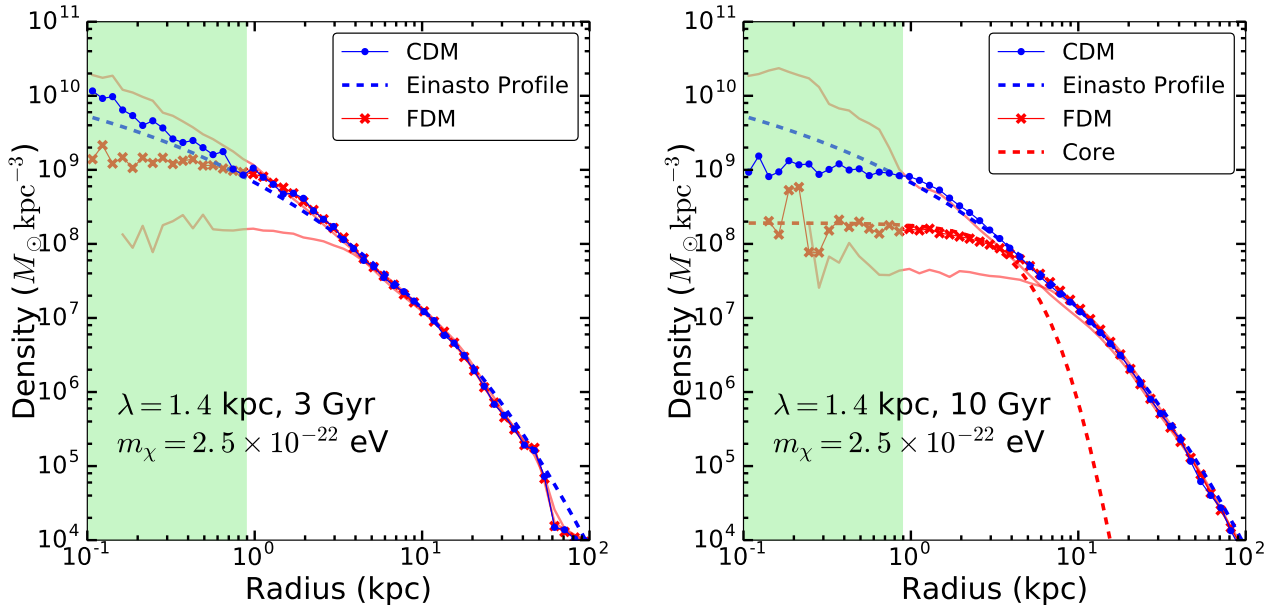


**Figure 4.** The left (right) panel is the halo density profile after 3 (10) Gyr. The two solutions of FDM without the correction factor  $\mathcal{B}_j$  (pink thin solid lines) are shown for reference. The green shaded region represents the radius of halo smaller than the softening length 0.89 kpc. The system is fully virialized after 10 Gyr. We can see that the FDM and CDM halo density profiles outside 10 kpc can both be fitted well by the Einasto profile. The density inside 1 kpc is lower than that of CDM halo after 3 Gyr and finally evolves into a solitonic core inside 4 kpc.

trust the results.

We plot two density profiles at 3 Gyr and 10 Gyr separately in Fig. 4. In the left panel, we show the density

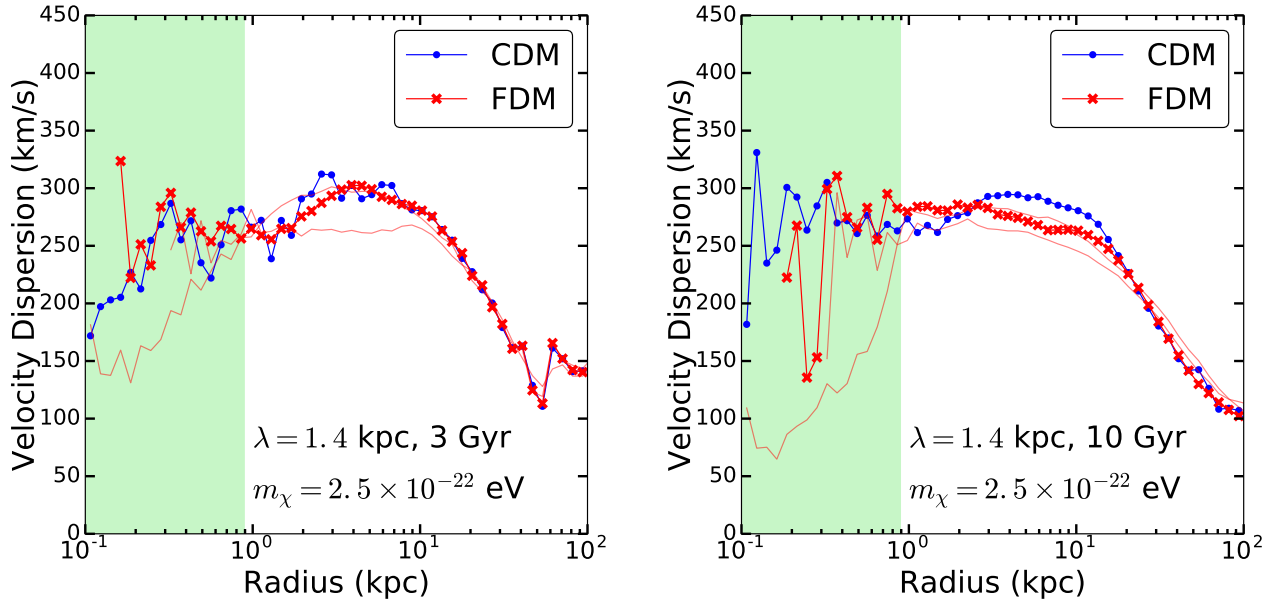


**Figure 5.** Left(right) panel: the velocity dispersion profiles at 3(10) Gyr. The two solutions of FDM without the correction factor  $\mathcal{B}_j$  (pink thin solid lines) are shown for reference. The green shaded region represents the radius of halo smaller than the softening length 0.89 kpc. Before final virialization, one cannot find significant difference between the FDM and CDM halos. The slight differences among the CDM and FDM halos around 10 kpc are still clear.

profiles for the FDM (red crosses) and CDM (blue circles) halos at 3 Gyr. Again, we plot the two solutions of FDM without the correction factor (pink thin solid lines) as reference. The green shaded region represents the region with radius smaller than the softening length 0.89 kpc. The halo is still not reaching the equilibrium at 3 Gyr time, and there is no significant difference between the CDM and FDM. We also plot the Einasto Profile fitting in the final virialized state in blue dashed line for comparison. At the region around 100 kpc, some particles are still bouncing out so that the tail is not fitted well to the Einasto profile. In the right panel, we show the density profiles at 10 Gyr. The fitting function of the solitonic core is shown in red-dashed line, the formula for which was given in Ref. (Schive et al. 2014b),

$$\rho_c(r) \simeq \rho_b \rho_0 [1 + 0.091 (\frac{r}{r_c})^2]^{-8}, \quad (24)$$

with an additional fitting parameter  $\rho_b$ , and

$$\rho_0 \simeq 3.1 \times 10^6 \left( \frac{2.5 \times 10^{-22} \text{ eV}}{m_\chi} \right)^2 \left( \frac{\text{kpc}}{r_c} \right)^4 \frac{M_\odot}{\text{kpc}^3}. \quad (25)$$

We set  $\rho_b = 5000$  and  $r_c = 3$  kpc in our plot. Beyond the solitonic core, the density profiles of FDM halos are essentially the same as that of CDM and the Einasto profile.

We confirm the existence of a solitonic core, slowly emerging from the FDM simulation, with a size of 3 kpc. Inside the solitonic core, our result agrees with the previous result obtained in Ref. (Schive et al. 2014b), which was based on a grid-based numerical solution of the Schrödinger-Poisson equations. Outside the solitonic core, our result agrees very well with the Einasto profile, which is also a well-known property of the FDM halo. In a previous study (Veltmaat & Niemeyer 2016), a boosted power in small scales was also reported for their small-box comoving coordinate simulation. Comparing to the CDM simulation, Ref. (Veltmaat & Niemeyer 2016) found at most 10% more power in the FDM simulation. We can now easily understand such a result by considering the quantum pressure in small scales.

We also compare the velocity dispersion profiles of the FDM (red lines) and CDM (blue line) halos after 3 Gyr (left panel) and after 10 Gyr (right panel) of evolution in Fig. 5. At 3 Gyr (left panel), we do not see significant differences between the FDM and CDM halos, except in the small central region less than the softening length.

However, the FDM velocity dispersion is smaller than that of CDM halo between 3 kpc and 20 kpc, both at 3 Gyr and at 10 Gyr, which can be understood as due to the lower mass enclosed within 3 kpc in FDM halos, as discussed in Fig. 3.

#### 4. SUMMARY AND OUTLOOK

In summary, we have proposed to use a Gaussian kernel function to discretize the quantum pressure term to simulate FDM in the PP method for  $N$ -body simulations. We note that the quantum pressure does not provide additional energy to the system, but it will certainly change the halo inner structure. In order to understand the quantum pressure effect, we study a two-body system and find that the force between the two particles is always attractive if the distance between them is less than  $\lambda/\sqrt{2}$ , but it will turn repulsive if the distance between them is larger than  $\lambda/\sqrt{2}$ . In small scales, the quantum pressure contribution can be even larger than gravity.

With our discretized quantum pressure approach to the PP method, we have constructed two  $N$ -body simulations, one for the CDM and the other one for the FDM, in a collapsing system with identical initial conditions. We found that the FDM halo center can be clearly distinguished from that of the CDM and also confirmed that a solitonic core forms at the FDM halo center, where the mass density is very flat, similar to the isothermal or Burkert profiles.

We have also compared the FDM halo evolution with the CDM case based on the mass enclosed within 8 kpc. We confirmed that the FDM halo will reach equilibrium slightly later than the CDM one while its galaxy formation history is consistent with current data (Hui et al. 2016).

Implied from the rotation curves, the FDM halo evolves into an inner solitonic core with either higher or lower density than the CDM if they started with identical initial condition; similar results can also be found in Ref. (Veltmaat & Niemeyer 2016).

The solitonic core we found in this work may not be able to quantitatively solve the cusp-core problem, but it is very suggestive that it may provide a solution if a full scale cosmological simulation is performed. One may worry that the non-linear effect from the attractive quantum pressure at the region less than one wavelength scale can bring higher mass density back to the center. This can be understood as the linear power-spectrum growth from the FDM model suppresses any power smaller than the FDM Jeans scale

$$\frac{2(\pi G\rho)^{1/4}m_\chi^{1/2}}{\hbar^{1/2}}.$$

However, we started our simulations for the CDM and FDM from the identical initial conditions, and the quantum pressure of the FDM suppresses the density for scales larger than one wavelength albeit boosts the density up in scales smaller than one wavelength. These two effects were also found in Ref. (Veltmaat & Niemeyer 2016) – the suppression of matter power spectrum from redshift  $z = 100$  to  $z = 16$  in small scales, but a boost of matter power spectrum at around  $z = 2$  in small scales.

We do not consider the cosmological simulation in this work but would like to return to this in the near future.

#### ACKNOWLEDGMENT

We would like to thank Volker Springel for some useful suggestion on the code, Tzi-Hong Chiueh for useful comments on the result. We acknowledge the help from ITSC in CUHK for providing computational resources for the project. This project is supported partially by grants from the Research Grant Council of the Hong Kong Special Administrative Region, China (Project No. C4047-14E) and the VC Discretionary Fund of CUHK. K.C. was supported

by the MoST under Grants No. MOST-105-2112-M-007-028-MY3.

## APPENDIX

### A. CORRECTION OF HIGH-NUMBER-DENSITY ENVIRONMENT

In the low-density limit, it is reasonable to assume that particles are dominantly under two-body force without the contribution from massive overlap terms. However, in high-number-density environment, our two-body interaction picture is no longer sufficient because of massive overlap contributions. In this section, we discuss our strategy to correct this issue.

From Eq. (18) and (19), if we take  $\mathcal{B}_j = 1$  we can see that the approximation

$$\left[ \sum_j m_j \delta(\mathbf{r} - \mathbf{r}_j) (\mathbf{r} - \mathbf{r}_j) \right]^2 \left[ \sum_j m_j \delta(\mathbf{r} - \mathbf{r}_j) \right]^{-1} \simeq \sum_j m_j \delta(\mathbf{r} - \mathbf{r}_j) (\mathbf{r} - \mathbf{r}_j)^2, \quad (\text{A1})$$

will not hold when we replace the delta function with the Gaussian kernel. Clearly, the approximation only works when the two-body interaction is dominant. In reality, a high-number-density system, e.g. in the center of a halo, has to be considered a more complicated system.

Let us start with a simple setup. Assuming  $N$  particles occupy a volume  $V$ , the average number density is  $N/V$  and the average distance  $D$  can be defined as  $(N/V)^{1/3}$ . In the limit of the average distance much larger than the matter wavelength  $D \gg \lambda$ , the probability for any particle pair to appear within one wavelength is given by

$$\mathcal{P}_0 \propto (\lambda/D)^3. \quad (\text{A2})$$

Extending the system to three particles, the probability of two particles being within one wavelength from one another will be proportional to  $\mathcal{P}_0^2$ . Similarly, the probability will be proportional to  $\mathcal{P}_0^{N-1}$  for a  $N$ -particle system. Thus, we can conclude that the sum of all pair-interactions can be a very good approximation (leading order) for an  $N$ -body system as long as  $D \gg \lambda$ .

On the other hand, if we consider the Gaussian kernel  $\mathcal{G}(\mathbf{r} - \mathbf{r}_i)$  in the limit of  $D \ll \lambda$ , it is no longer accurate to ignore the overlap between the Gaussian tails. Such next-to-leading order contributions can be very significant if we add up all the tail interactions of the  $N$ -body system. Hence, we propose a numerical correction factor  $\mathcal{B}_j$  to account for such additional interactions. To estimate the value of  $\mathcal{B}_j$  whose index  $j$  denotes the label of tree-node, we have to unfold the tree-method back to Eq. (16). Therefore, we can first define  $\mathcal{B}_j$  (for each  $j$ ) to be the net effect of Gaussian tails of all the individual simulation particles  $i$ ,

$$\left[ \sum_i m_i \mathcal{G}(\mathbf{r} - \mathbf{r}_i) (\mathbf{r} - \mathbf{r}_i) \right]^2 \left[ \sum_i m_i \mathcal{G}(\mathbf{r} - \mathbf{r}_i) \right]^{-1} = \mathcal{B}_j \sum_i m_i \mathcal{G}(\mathbf{r} - \mathbf{r}_i) (\mathbf{r} - \mathbf{r}_i)^2. \quad (\text{A3})$$

We can rewrite the left hand side of Eq. (A3) to be

$$\frac{\sum_{i=1}^N m_i^2 \mathcal{G}^2(\mathbf{r} - \mathbf{r}_i) (\mathbf{r} - \mathbf{r}_i)^2 + 2 \sum_{i \neq i'} m_i m_{i'} \mathcal{G}(\mathbf{r} - \mathbf{r}_i) \mathcal{G}(\mathbf{r} - \mathbf{r}_{i'}) [(\mathbf{r} - \mathbf{r}_i) \cdot (\mathbf{r} - \mathbf{r}_{i'})]}{\sum_{i=1}^N m_i \mathcal{G}(\mathbf{r} - \mathbf{r}_i)}. \quad (\text{A4})$$

We can see that the major difference between the left hand side (LHS) and right hand side (RHS) of Eq. (A3) mainly comes from the overlap terms, which can be amplified for  $N$  particles. Thus, we can guess that the factor  $\mathcal{B}_j$  is proportional to  $N \sim (D/\lambda)^3$ . However, finding the exact form for  $\mathcal{B}_j$  is not so trivial. Here we can perform a Monte-Carlo simulation in the range of  $D/\lambda$  from zero to infinity to compute exactly the value of the LHS and RHS of Eq. (A3), and then a proper fitting function for  $\mathcal{B}_j$  can be obtained.

In the following, we list the procedures of such a Monte-Carlo simulation.

1. Generate a large number of particles randomly distributed in a cubic box. The length of box side is much larger than the matter wavelength  $\lambda$ .

2. Calculate the values of the LHS and RHS of Eq. (A3) with  $\mathcal{B}_j = 1$  at the center of the box.
3. Compare the two values computed in step 2 and calculate the value of  $\mathcal{B}_j$  with respect to  $D/\lambda$ .
4. Repeat the previous steps with different numbers of particles, different box sizes and different  $\lambda$ 's to ensure the convergence of the results.

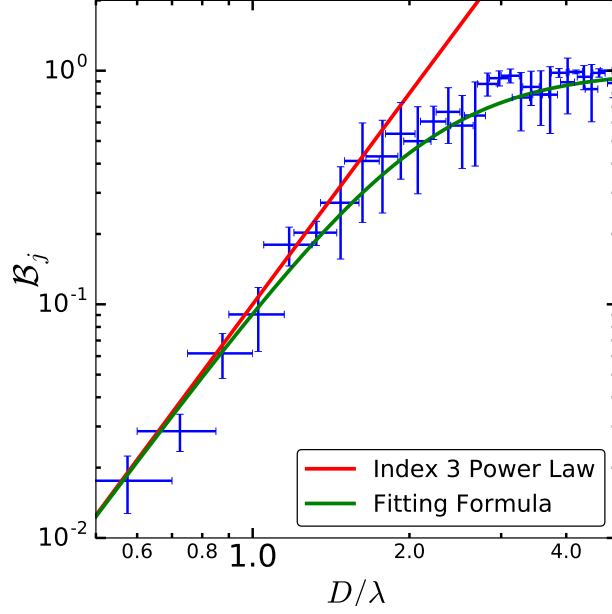


**Figure A1.** Simulation results are shown in blue errorbars. The red solid line is the power law with power-index=3. The green solid line is the fitting formula we give in (A5). The errorbars in the x-axis are given by the bin size. The errorbars in the y-axis are given by the standard deviation of  $\mathcal{B}_j$  in the bins.

We present our simulation results in Fig. A1 and fit the data with a formula

$$\mathcal{B}_j = (D/\lambda)^3 / (10 + (D/\lambda)^3). \quad (\text{A5})$$

The error bars of each data point originate from the standard deviation of different scans. As expected, the  $\mathcal{B}_j$  approaches the value about 1 at the region of very large  $D/\lambda$ , but is almost linearly increasing in the log-log scale in the region  $D < 2\lambda$ . The fitting formula (A5) provides us the correction of the quantum pressure in the densest region in the simulation, for example at the center of halos.

#### A.1. Numerical implementation of quantum pressure and its corrections in the Tree algorithm

Gadget2 (Springel 2005) is a TreePM hybrid N-body code and the correction factor  $\mathcal{B}_j$  has to be implemented in the Tree data structure. In the following, we list the basic procedures of the new implementation.

1. We build a tree structure to save the information of particle distribution.
2. For each simulation particle, we calculate the gravitational force from the tree nodes.
3. The quantum pressure from the same tree nodes are also computed in the same time and same numerical loop.
4. The local particle number density information can be taken from the tree so that the correction factors  $\mathcal{B}_j$  can be calculated accordingly.

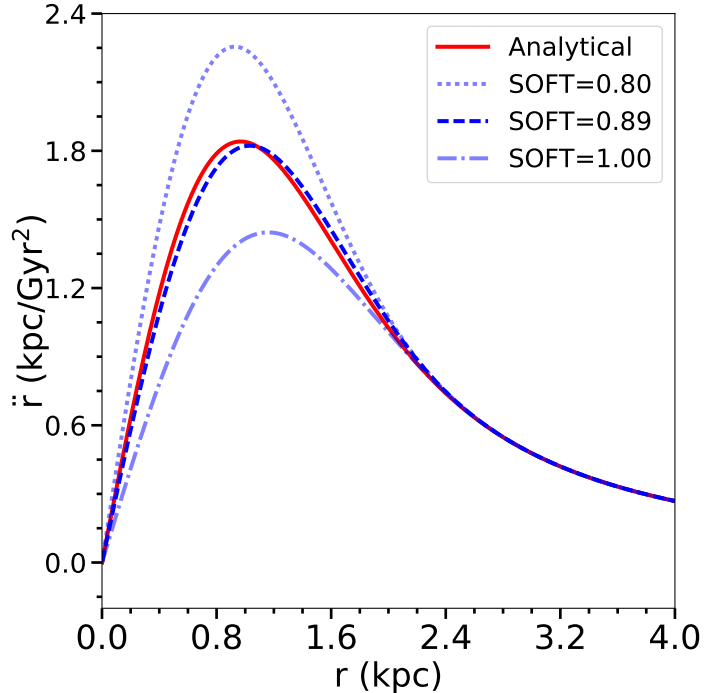


**Figure B2.** The red curve is the analytical form of gravitational acceleration from a gaussian density distribution. The blue dashed curve is the best fit for `SOFT = 0.89` kpc, where `SOFT` is short for the softening length option `SofteningHalo`. The other two light blue curves are `SOFT = 0.8` kpc (upper, dotted) and `SOFT = 1.0` kpc (lower, dot-dashed).

5. To avoid breaking Newton’s third law, we also take the particle number density for the father node of the particle into account. Such an action properly keeps the density around the particle and the tree node smooth without sharp artificial cuts, which could break the Newton’s third law.

In principle, the computational time for a FDM simulation is about twice as much as that for a classical gravity only CDM simulation. In fact, among our tests the FDM simulation costs two to three times as much as the CDM one. When particles are close to each other, the quantum pressure can be larger than gravity to keep the accuracy of acceleration, velocity and position calculation. It turns out that all time steps are adaptively shortened than the one without quantum pressure.

## B. SOFTENING LENGTH AND KERNEL SIZE

The gravitational softening length (option `SofteningHalo` in `Gadget2`) is a critical numerical parameter for N-body simulation because it can avoid approaching the singularity when the distance between two particles becomes very small. In addition, some softening lengths within a certain volume can help to maintain the correct gravity force. Ideally, if one could use infinite numbers of particles to represent the fluid, then the softening length would be zero. However, in our FDM simulations, the softening length cannot be zero nor a completely artificial parameter because the density distribution is defined by the Gaussian kernel. Unlike CDM, the FDM softening length is strongly related to the matter wavelength. In this appendix, we estimate the softening length as a function of the wavelength  $\lambda$ .

For a distribution of mass with Gaussian density distribution, the gravitational acceleration acting on a test particle is

$$\ddot{\mathbf{r}} = \frac{GM(< r)}{r^3} \mathbf{r}, \quad (\text{B6})$$

where  $M(< r)$  is the mass enclosed in the radius  $r$  from the center of the Gaussian kernel. The mass enclosed in the

radius  $r$  can be re-parameterized as

$$\frac{M(< r)}{M(r = \infty)} = \frac{\int_0^r \exp\left(\frac{-2r^2}{\lambda^2}\right) 4\pi r^2 dr}{\int_0^\infty \exp\left(\frac{-2r^2}{\lambda^2}\right) 4\pi r^2 dr} = \operatorname{erf}\left(\frac{\sqrt{2}r}{\lambda}\right) - 1.13 \exp\left(\frac{-2r^2}{\lambda^2}\right) \frac{\sqrt{2}r}{\lambda}. \quad (\text{B7})$$

In Fig. B2, we present various gravitational acceleration (blue dashed lines) by taking into account different softening lengths, also see Eq. (4) in Ref. Springel (2005).

We also show the analytical curve (red solid line) that is computed by assuming the Gaussian kernel density distribution described in Eq. (B7). Clearly, the softening length  $\text{SOFT} = 0.89 \text{ kpc}$  gives the best fit to the analytical curve, yet  $\text{SOFT} = 0.8 \text{ kpc}$  or  $\text{SOFT} = 1 \text{ kpc}$  differ by less than 50%. Therefore, we use the best-fit value of softening length  $0.89 \text{ kpc}$  in the simulation. The wavelength  $\lambda = 1.4 \text{ kpc}$  has been chosen in this work, nevertheless,  $\lambda$  and the softening length  $\text{SOFT} = 0.89 \text{ kpc}$  are correlated in this context.

### C. VERIFICATION OF PARTICLE-PARTICLE SIMULATION

In this section, our PP method is verified with some simple one-dimensional simulations by comparing with other methods such as the PM method and the approach introduced in (Veltmaat & Niemeier 2016). We first perform the simulations based on the PP and PM methods. The same initial conditions are applied: two particles located 10 distance units away from each other and the density distribution smoothed by Gaussian kernels. For the sake of simplicity, we turn off the gravitational potential so that the acceleration of the particles is only caused by the QP.

In the PP simulation, we adopt the acceleration of particle described by Eq. (23) and then evolve the particles with the iteration relations

$$x_{t+\delta t} = x_t + v_t \delta t + \frac{1}{2} a_t (\delta t)^2, \quad v_{t+\delta t} = v_t + \frac{1}{2} a_t \delta t, \quad (\text{C8})$$

where  $x_t$ ,  $v_t$  and  $a_t$  are the position, velocity and acceleration of the particle at time  $t$ , respectively. The size of the time step is given by an adjustable value of  $\delta t$  in order to achieve adequate accuracy.

In the PM simulation, the acceleration  $a_t$  is  $-\nabla Q$  based on the original definition. The acceleration  $-\nabla Q$  shall be computed for each bin. To handle the  $\nabla^2 \sqrt{\rho}$  in the QP given by Eq. (7), the three-point function is engaged to numerically calculate second order derivative,

$$f''(x) = \lim_{h \rightarrow 0} \frac{f(x+h) - 2f(x) + f(x-h)}{h^2},$$

where  $h$  is the bin size. However, we adopt the two-point function

$$f'(x) = \lim_{h \rightarrow 0} \frac{f(x+h) - f(x-h)}{2h},$$

for calculating  $-\nabla Q$ . We have carefully checked the convergence of the simulations with different values of  $\delta t$  and  $h$ . With the values  $\delta t = 0.01$  units of time and  $h = 0.05$  units of distance, the result is stable for illustration.

The comparison of PP and PM results for the correlation between acceleration and position of a particle is demonstrated in Fig. C3. The thick red solid line presents the PM result and the thick cyan solid line is for the PP result. One can decompose the PM simulation result into the lowest frequency mode ( $N = 1$ ), high frequency mode ( $N = 2$ ) and noise, corresponding to the dark green dot-dashed line, purple dashed line and light green dashed line, respectively. From Appendix B of Ref. (Hui et al. 2016), we recognize that the lowest frequency mode is actually related to the lowest eigenstate of the Schrödinger-Poisson equation (ground state  $N = 1$ ), and the contribution of the lowest eigenstate of Schrödinger-Poisson equation is larger than other eigenstates in the density of the halo. Importantly, we found that the PP simulation result is dominated by the lowest frequency mode, which can be seen from the small difference between thick blue solid line and dark green dashed line.

There is no doubt that the lowest frequency mode is more significant than higher frequency modes because the higher frequency modes are nearly averaged out in each interval. This fact implies that our PP method for FDM

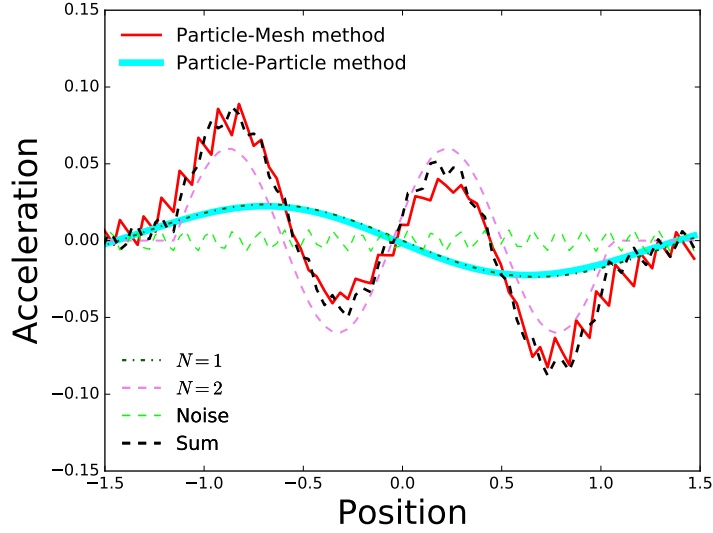


**Figure C3.** Acceleration versus position of one particle in different situations. Here the thick red solid line is from the simulation with the PM method, while the thick cyan solid line is from the simulation with the PP method. The result of the simulation with the PM method can be decomposed into two modes ( $N = 1$  and  $N = 2$ ) together with numerical noise. The result of the simulation with the PP method is indeed the lowest frequency mode ( $N = 1$ ). The dark green dot-dashed line, purple dashed line and light green dashed line are the lowest frequency mode ( $N = 1$ ), the high frequency mode ( $N = 2$ ) and the noise, respectively.

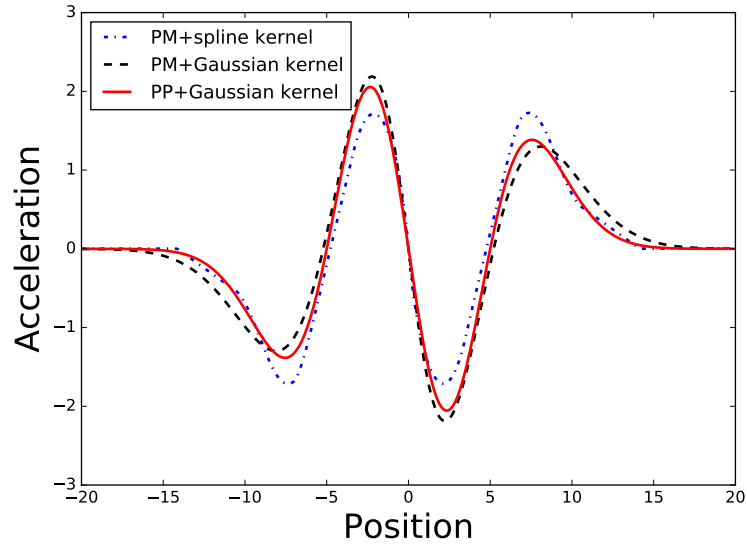


**Figure C4.** Comparison of the result of acceleration from our method with the method in Ref. (Veltmaat & Niemeyer 2016) and the usage of kernel in Ref. (Veltmaat & Niemeyer 2016). The red solid line is the result of our PP method, the black dashed line is the result of the method in Ref. (Veltmaat & Niemeyer 2016) with a Gaussian kernel and the blue dash-dotted line is the result of the method in Ref. (Veltmaat & Niemeyer 2016) with a spline kernel (the kernel used in Ref. (Veltmaat & Niemeyer 2016)).

simulation is only able to capture the ground state component, nevertheless it is the most dominant component. Hence, such a PP method for FDM simulation is a good approximation and helps to reduce the simulation cost and complexity. There could be a very small error near the boundary of the softening length due to the omitted higher frequency modes when using our PP method. However, it is just a tiny effect on the large scale structure in a cosmological simulation because there is much weaker QP due to the larger simulation particle mass.

Next, we compare our PP method with the method developed in Ref. (Veltmaat & Niemeyer 2016). Again, we place two particles symmetrically and give them tiny initial velocity to make them move towards each other. We record the acceleration of one of the particles in the process as shown in Fig. C4. In the simulation, we use the leapfrog algorithm to impose the acceleration on each particle and follow their movement.

The red solid line is the acceleration versus position curve recorded with the PP method. The black dashed and blue dash-dotted lines are recorded with the method developed in Ref. (Veltmaat & Niemeyer 2016) but using the Gaussian and spline kernels, respectively. For convenience, we called the kernel used in Ref. (Veltmaat & Niemeyer 2016) as spline kernel. Our PP method gives a similar acceleration versus position curve as that in Ref. (Veltmaat & Niemeyer 2016), despite of the different choices of the kernel. We also found that the Gaussian kernel is rather suitable for the QP calculation since the spline kernel is not smooth after performing first order derivative.

We conclude that our PP method is consistent with a previous PM method Ref. (Veltmaat & Niemeyer 2016) in the aspect of QP calculation. Moreover, our PP method captures the lowest frequency mode of the QP, whose resolution and accuracy are enough for a cosmological simulation. The further improvement of our method will lie in considering additional factors such as anisotropic kernel and higher frequency modes. We will study these possible improvements in the future.

## REFERENCES

- Aaboud, M., et al. 2016, *Phys. Rev.*, D94, 032005  
Aartsen, M. G., et al. 2016, *Eur. Phys. J.*, C76, 531  
Ackermann, M., Albert, A., Anderson, B., et al. 2015, *Physical review letters*, 115, 231301  
Akerib, D. S., et al. 2016, arXiv:1608.07648  
Amendola, L., & Barbieri, R. 2006, *Physics Letters B*, 642, 192  
Boehmer, C. G., & Harko, T. 2007, *JCAP*, 0706, 025  
Boylan-Kolchin, M., Bullock, J. S., & Kaplinghat, M. 2011, *Mon. Not. Roy. Astron. Soc.*, 415, L40  
Bozek, B., Marsh, D. J., Silk, J., & Wyse, R. F. 2015, *Monthly Notices of the Royal Astronomical Society*, 450, 209  
Calabrese, E., & Spergel, D. N. 2016, *Monthly Notices of the Royal Astronomical Society*, 460, 4397  
Chavanis, P.-H. 2011, *Physical Review D*, 84, 043531  
Chavanis, P.-H., & Delfini, L. 2011, *Physical Review D*, 84, 043532  
CMS. 2016  
de Blok, W. J. G. 2010, *Adv. Astron.*, 2010, 789293  
Dev, P., Lindner, M., & Ohmer, S. 2016, arXiv preprint arXiv:1609.03939  
Du, X., Behrens, C., & Niemeyer, J. C. 2016, arXiv preprint arXiv:1608.02575  
Ferrer, F., & Grifols, J. A. 2004, *JCAP*, 0412, 012  
Goodman, J. 2000, *New Astron.*, 5, 103  
Guzmán, F. S., & Ureña-López, L. A. 2003, *Physical Review D*, 68, 024023  
Hložek, R., Marsh, D. J. E., Grin, D., et al. 2017, *Phys. Rev.*, D95, 123511  
Hu, W., Barkana, R., & Gruzinov, A. 2000a, *Phys. Rev. Lett.*, 85, 1158  
—. 2000b, *Physical Review Letters*, 85, 1158  
Hui, L., Ostriker, J. P., Tremaine, S., & Witten, E. 2016, arXiv:1610.08297  
Kim, J. E., & Marsh, D. J. 2016, *Physical Review D*, 93, 025027  
Klypin, A. A., Kravtsov, A. V., Valenzuela, O., & Prada, F. 1999, *Astrophys. J.*, 522, 82  
Lee, J.-W., & Lim, S. 2010, *JCAP*, 1001, 007  
Marsh, D. J. 2016, *Physics Reports*, 643, 1  
Marsh, D. J. E. 2015, *Phys. Rev.*, D91, 123520  
Matos, T., Guzmán, F. S., Ureña-López, L. A., & Núñez, D. 2002, in *Exact Solutions and Scalar Fields in Gravity* (Springer), 165–184  
Mielke, E. W., & Perez, J. A. V. 2009, *Phys. Lett.*, B671, 174  
Mocz, P., & Succi, S. 2015, *Physical Review E*, 91, 053304  
Moore, B., Ghigna, S., Governato, F., et al. 1999, *Astrophys. J.*, 524, L19  
Peebles, P. J. E. 2000, *Astrophys. J.*, 534, L127  
Press, W. H., Ryden, B. S., & Spergel, D. N. 1990, *Phys. Rev. Lett.*, 64, 1084  
Schaller, M., Frenk, C. S., Bower, R. G., et al. 2015a, *Mon. Not. Roy. Astron. Soc.*, 451, 1247  
—. 2015b, *Mon. Not. Roy. Astron. Soc.*, 452, 343  
Schive, H.-Y., Chiueh, T., & Broadhurst, T. 2014a, *Nature Physics*, 10, 496  
Schive, H.-Y., Liao, M.-H., Woo, T.-P., et al. 2014b, *Physical review letters*, 113, 261302  
Schwabe, B., Niemeyer, J. C., & Engels, J. F. 2016, *Physical Review D*, 94, 043513  
Sikivie, P., & Yang, Q. 2009, *Phys. Rev. Lett.*, 103, 111301  
Sin, S.-J. 1994, *Phys. Rev.*, D50, 3650  
Spiegel, E. 1980, *Physica D: Nonlinear Phenomena*, 1, 236  
Springel, V. 2005, *Monthly Notices of the Royal Astronomical Society*, 364, 1105  
Tan, A., Xiao, M., Cui, X., et al. 2016, *Physical Review Letters*, 117, 121303  
Tulin, S., Yu, H.-B., & Zurek, K. M. 2013, *Phys. Rev.*, D87, 115007  
Turner, M. S. 1983, *Phys. Rev.*, D28, 1243  
Uhlemann, C., Kopp, M., & Haugg, T. 2014, *Phys. Rev.*, D90, 023517  
Veltmaat, J., & Niemeyer, J. C. 2016, arXiv preprint arXiv:1608.00802